Fluorescent Nanowire Ring Illumination for Wide-Field Far-Field Subdiffraction Imaging

Xiaowei Liu,[1] Cuifang Kuang,[1] Xiang Hao,[1] Chenlei Pang,[1] Pengfei Xu,[1] Haifeng Li,[1] Ying Liu,[2] Chao Yu,[1] Yingke Xu,[3] Di Nan,[3] Weidong Shen,[1] Yue Fang,[1] Lenian He,[4] Xu Liu,[1,†] and Qing Yang[1,*]

[1]*State Key Laboratory of Modern Optical Instrumentation, College of Optical Science and Engineering, Zhejiang University, Hangzhou 310027, China*

[2]*School of Materials Science and Engineering, Georgia Institute of Technology, Atlanta, Georgia 30332-0245, USA*

[3]*Key Laboratory for Biomedical Engineering of the Ministry of Education, Department of Biomedical Engineering, Zhejiang University, Hangzhou 310027, China*

[4]*Institute of VLSI Design, Zhejiang University, Hangzhou 310027, China*

(Received 22 September 2016; revised manuscript received 22 November 2016; published 14 February 2017)

Here we demonstrate an active method which pioneers in utilizing a combination of a spatial frequency shift and a Stokes frequency shift to enable wide-field far-field subdiffraction imaging. A fluorescent nanowire ring acts as a localized source and is combined with a film waveguide to produce omnidirectional illuminating evanescent waves. Benefitting from the high wave vector of illumination, the high spatial frequencies of an object can be shifted to the passband of a conventional imaging system, contributing subwavelength spatial information to the far-field image. A structure featuring 70-nm-wide slots spaced 70 nm apart has been resolved at a wavelength of 520 nm with a 0.85 numerical aperture standard objective based on this method. The versatility of this approach has been demonstrated by imaging integrated chips, Blu-ray DVDs, biological cells, and various subwavelength 2D patterns, with a viewing area of up to 1000 μm^2, which is one order of magnitude larger than the previous far-field and full-field nanoscopy methods. This new resolving technique is label-free, is conveniently integrated with conventional microscopes, and can potentially become an important tool in cellular biology, the on-chip industry, as well as other fields requiring wide-field nanoscale visualization.

DOI: 10.1103/PhysRevLett.118.076101

The resolution of conventional optical imaging systems is limited by their inabilities to capture exponentially decaying evanescent waves in the near field, which carry subwavelength spatial information about the objects being examined. While nanoscopy has been greatly improved by labeling techniques [1–4], the development of label-free subdiffraction imaging, which is significant for antirejection and chromophore-incompatible conditions, remains rather slow. In particular, near-field scanning optical microscopy has achieved spatial resolutions down to ~20 nm by scanning objects using a nanotip in the near field [5–12]. However, to avoid invasion and perturbance, breaking the diffraction limit in the far field is highly desirable [13–18]. Recent developments in hyperlens and microsphere contacting technologies to achieve label-free far-field subwavelength resolution have brought new opportunities but still face the limitations of a confined spectral range and a small field of view (FOV), respectively [13,14,19]. Achieving wide-field, label-free optical images for diverse subwavelength objects in the far field would be a significant breakthrough, with promising applications in biology, chemistry, and physics.

One-dimensional (1D) nanomaterials have shown great promise for high-sensitivity and high-resolution detection and imaging, which are widely applied in areas including communication, diagnosis, and environmental monitoring [5,6,20]. The 1D nanomaterial-based light emitters, owing to their strong light localization [21,22], ultrasmall footprint [23], high mechanical flexibility [24], large aspect ratio [25,26], and large fractional evanescent field [27], could be used to break the bottleneck in nanoscopy and allow wide-field far-field subdiffraction imaging at multiple wavelengths [28,29].

In our design of nanowire ring (NWR) illumination microscopy (NWRIM), a fluorescent NWR acts as a localized source and is combined with a film waveguide to produce omnidirectional evanescent waves with large transverse wave vectors (TWVs) to interact with an object in a wide area. The high spatial frequencies of the object can be shifted to the central position of the frequency domain, in the passband of a conventional imaging system (S2.1 [30]). Consequently, the final wide-field image captures fine features of the object and possesses an enhanced resolution. The ring-shaped light source enables a 2D spatial frequency shift for 2D imaging. The Stokes frequency shift between the NW's fluorescence and the pumping laser enables the pumping laser to be filtered for a high signal-to-noise-ratio (SNR). Furthermore, the high luminescence efficiency and high mechanical flexibility of the semiconductor NWs make this NWRIM efficient and reliable for subdiffraction imaging [31–33].

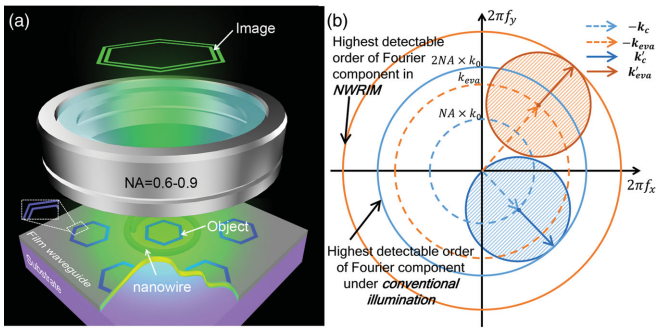

FIG. 1. Schematic of the NWRIM. (a) Schematic of the configuration and imaging process. A hexagon array is used as an example object to show the effect of NWRIM. Under an omnidirectional evanescent illumination from the fluorescent NWR, the subdiffraction nested features of the central hexagon show up in the far-field image. (b) The basic mechanism of the NWRIM method. $\mathbf{k_c}$ and $\mathbf{k'_c}$ are the TWVs of the illuminating and scattered light, respectively, under conventional illumination. $\mathbf{k}_{\mathrm{eva}}$ and $\mathbf{k'}_{\mathrm{eva}}$ are the TWVs of the illuminating and scattered light, respectively, under NWR evanescent illumination.

Figure 1(a) shows the schematic of the NWRIM. A semiconductor NWR is placed on a subwavelength film waveguide. When the NW is pumped, fluorescent light effectively couples to and propagates in the underlying film. Because of the nanoscale thickness of the film, a high proportion of the evanescent wave distributes on the top surface during the light propagation [27] (Fig. S13). The object on the film surface perturbs the propagation of the evanescent wave, and the scattered light is collected by a far-field objective. We can analyze the interaction between the object and incident evanescent wave as follows. The object is considered as a superposition of a series of sine or cosine gratings that would give "momentum" to the incident photons. The TWV of the output light can be calculated by

$$k' = k + 2\pi\Lambda, \tag{1}$$

where Λ is the spatial frequency of one grating component and k is the TWV of the input light. A grating component with a larger spatial frequency corresponds to finer structures in the object. Considering a grating with a spatial frequency Λ larger than $1/\lambda$, the output TWV is greater than $2\pi/\lambda$ if the incident TWV is very small compared with $2\pi\Lambda$. The output light turns out to be a near-field evanescent wave. In NWRIM, the TWV of the incident wave is $2\pi n_{\mathrm{eff}}/\lambda$, which can offset $2\pi\Lambda$ when n_{eff} is high enough (n_{eff} is the effective refractive index of the propagation mode in the film waveguide). The output light with a small TWV sum is able to reach the far field for detection as a propagation wave.

Using the Ewald sphere of reflection [34], the relationship between the detected scattered light and the spatial features of the object can be expressed by

$$A(\mathbf{k}', \mathbf{k}) = P\left(\frac{|\mathbf{k}'|}{NA \times k_0}\right) \times F(\mathbf{k}' - \mathbf{k}), \tag{2}$$

where $k_0 = 2\pi/\lambda$, $\mathbf{k}$ is the TWV of the incident illumination wave, $\mathbf{k}'$ is the TWV of the scattered light, $A(\mathbf{k}', \mathbf{k})$ is the amplitude of the scattered light which can be detected in the far field, NA is the numerical aperture of the objective, $P(|\mathbf{k}'|/NA \times k_0)$ is nonzero only when $|\mathbf{k}'| < \mathrm{NA} \times k_0$, and $F(\mathbf{k}' - \mathbf{k})$ is the Fourier spectrum of the object's scattering potential at $(\mathbf{k}' - \mathbf{k}/2\pi)$. The range of $\mathbf{k}' - \mathbf{k}$ that satisfies a nonzero $A(\mathbf{k}', \mathbf{k})$ is marked by shadow circles in Fig. 1(b), for a conventional illumination (blue) and an evanescent wave illumination (orange), respectively. In conventional illumination, both the incident and collected directional vectors are confined by the NA of the conventional imaging system. Consequently, the far-field detectable Fourier components are limited to a circle with radius of $2\mathrm{NA} \times k_0$ [larger blue circle in Fig. 1(b)]. The loss of the high order of Fourier components leads to a loss of detailed information during the imaging process. While under evanescent wave illumination with the TWV $\mathbf{k}_{\mathrm{eva}}$, the spatial frequencies carried by the far-field scattered field are centered at $(-\mathbf{k}_{\mathrm{eva}}/2\pi)$. The highest detectable spatial frequencies are enlarged, as shown by the larger orange circle with a radius of $|-\mathbf{k}_{\mathrm{eva}}|/2\pi + \mathrm{NA}/\lambda$ in Fig. 1(b). Consequently, a higher resolution can be achieved.

We have used several types of materials with different refractive indices as the subwavelength film waveguide, including SiO_2, Al_2O_3, and TiO_2. Figure 2(a) shows an 85 nm slot structure with 85 nm spacing on 200-nm-thick Al_2O_3 film. The center-to-center distance between the two slots is much below the conventional diffraction-limited resolution ($R = 373$ nm) but well resolved under a CdS NW illumination [Fig. 2(b), $\lambda = 520$ nm]. The scattered field is shown in Figs. 2(d) and 2(e). The Fourier transformation of the scattered field [Fig. 2(g)] is the same as the object's spatial frequencies centered at $(-k_{\mathrm{eva}}/2\pi, 0)$ [orange circle in Fig. 2(f)]. The far-field image calculated based on the scattered field [35] (S1.3) shows the slot-pair feature in Fig. 2(h), quite consistent with the experimental results. The simulations verify that the frequency shift effect contributes to the high resolution of the experimental observations. After a deeper analysis, we find that, under the evanescent wave illumination, the image amplitude of a subwavelength slot pair can be approximated as

$$I(x) = A(x) + \exp(iak_{\mathrm{eva}}) \times A(x - a), \tag{3}$$

where $A(x)$ is the image amplitude of a single slot under evanescent wave illumination, and a is the center-to-center distance between the two slots. When $\pi/2k_{\mathrm{eva}} < a < 3\pi/2k_{\mathrm{eva}}$, the evanescent wave-matter interaction leads to an intensity valley between the two slots, which makes them resolvable (S2.2). And a magnification is possible, resulting in a wider imaging interval between the two slots [Fig. 2(i)]. The reconstructed image that involves both the low and high spatial frequencies has the same interval distance as the object, as well as a high resolution (Figs. S23 and S24). This analysis of slot-pair images would work equally well for

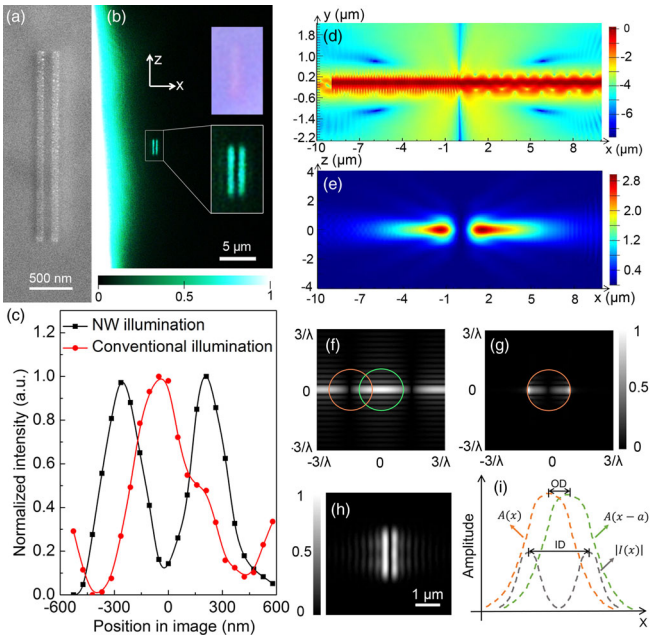

FIG. 2. Imaging of a pair of 85-nm-wide slots spaced 85 nm apart on an Al_2O_3-SiO_2-Si substrate. (a) Scanning electron microscopy (SEM) image of the slot pair. (b) Far-field optical microscopy image of the slot pair under NW illumination. The images under NW illumination (lower inset) and conventional illumination (upper inset) are magnified for clarity. NA = 0.85. (c) Cross-sectional intensity distribution of images under NW illumination (black curve) and conventional illumination (red curve). (d) Simulated cross-sectional view of the near field to far-field scattering process. The field intensity is shown on a log scale. (e) Far-field electromagnetic field distribution (2 μm above the object plane) of the scattered light. (f) Frequency spectrum of the slot pair. The green and orange circles are centered at (0, 0) and $(-k_{\mathrm{eva}}/2\pi, 0)$, respectively. Their radius is $1/\lambda$. (g) Fourier transformation of the scattered light. (h) Simulated far-field image with an ideal aberration-free 0.85 NA imaging system. (i) Schematic of the amplitude distribution of the image for each slot (green and orange lines) and the total image (gray line). OD and ID are abbreviations for "object distance" and "image distance," respectively.

dot-pair images. We note that this evanescent wave-structure interaction is unlike the destructive interference between different modes in nanoantennas or nanocavities. It barely depends on the size of each subwavelength slot (Figs. S6 and S7), whereas the nanoantenna effect is strongly size dependent [36]. We have also successfully resolved a trislot structure (130 nm slot, 130 nm spacing) on the Al_2O_3 film (Fig. S17) under 700 nm wavelength evanescent wave illumination (NA = 0.75). A higher film refractive index leads to a higher TWV of the evanescent wave and thus increases the shift value in the spatial frequency spectrum and hence the potential resolution. A slot pair with 70 nm slot and 70 nm spacing is clearly resolved on a 150-nm-thick TiO_2 film, with an imaging magnification factor up to ×3.2 (Fig. S9). According to our simulation, the finest resolvable center-to-center distance on a 200-nm-thick TiO_2 film is 70 nm under a ZnO NW illumination (Table S2 in S3.1).

NWRIM is applicable not only to objects embedded in the film but also to objects placed on it. A subdiffraction image was successfully achieved for a ridge-pair structure (Fig. S18). Further comparison experiment with a damaged film surface proved the key to achieving subdiffraction imaging is the effective coupling of fluorescent light into the film as an evanescent or guided field (Fig. S11).

To achieve subdiffraction resolution in a wide FOV, the photoluminescence of the NW plays an indispensable role. When the NW functions as a passive waveguide, the evanescent wave is confined near the NW and can illuminate only patterns in its vicinity [Figs. 3(a) and S10] [37]. However, when the NW actively fluoresces, the emission couples to the underlying film and propagates radially to cover a much broader view [Figs. 3(b)–3(d)]. Table S1 (see S2.4) lists some main parameters for recently reported far-field label-free nanoscopy. The FOV of NWRIM is at least one order of magnitude larger than the other kind of techniques.

As discussed, the high spatial frequency can be shifted to enhance the resolution along the incident direction of the evanescent wave. However, to achieve 2D subdiffraction imaging, the illuminating wave vectors should cover all the directions in the object plane. A limited incident range leads to incomplete imaging [Fig. 4(b)]. Thanks to the high aspect ratio and high flexibility of semiconductor NWs, an illumination covering all angles can be easily realized by circling the NW around the observed object. We have conducted ring illumination experiments on different films for various 2D patterns [Figs. 4(c),4(e), and 4(g)]. Subwavelength feature sizes are resolved in these 2D subdiffraction images, such as the 76 nm slots and 76 nm spacing of a "ZJU" pattern. Additionally, an optimal diameter of the NWR can ensure the illumination uniformity and a low background, which is dependent on the light propagation in the film waveguide. For a SiO_2 film coating on Si substrate, an NWR diameter around 10 μm is best (Fig. S14). Compared with the SiO_2-Si substrate, the Al_2O_3-SiO_2-Si bilayer substrate can propagate more stable

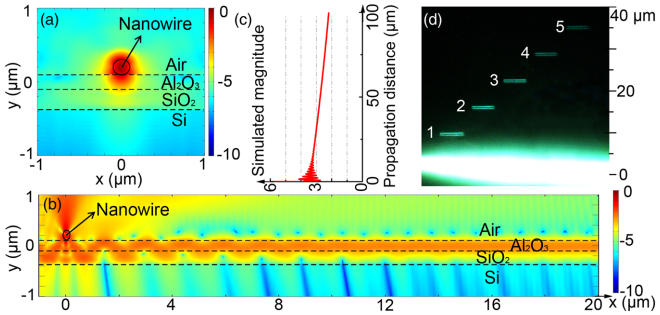

FIG. 3. (a),(b) Simulated cross-sectional field distribution when the NW works (a) passively and (b) actively on an Al_2O_3-SiO_2-Si substrate, respectively. Intensity is shown on a log scale. (c) Simulated field magnitude in the Al_2O_3 film along the propagation direction. (d) Image of a stair-shaped slot-pair array under NW illumination.

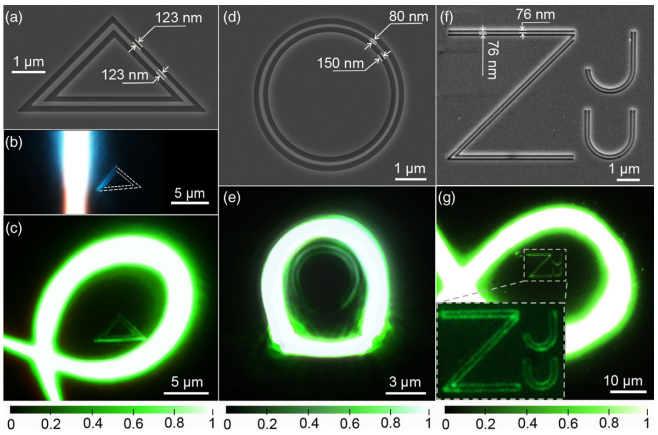

FIG. 4. NWRIM images of various fabricated 2D patterns with subwavelength features. (a)–(c) SEM image (a) of a triangular pattern on a SiO_2 film and its images under illumination from a straight NW (b) and an NWR (c), respectively. NA = 0.75. Lines perpendicular or nearly perpendicular with the NW fail to be imaged in (b). (d),(e) SEM (d) and NWRIM (e) images of a circular pattern on an SiO_2 film. NA = 0.75. (f),(g) SEM (f) and NWRIM (g) images of an arbitrary ZJU pattern on an Al_2O_3 film. NA = 0.85.

evanescent waves and the NWR diameter can be enlarged to 40 μm in experiments [Figs. 3(d) and S15]. The theoretical propagation distance is much larger [Fig. 3(c)], and we expect an improved ring diameter and FOV by optimizing the film quality in the future.

It is noteworthy that NWRIM is different from total internal reflection fluorescence (TIRF) microscopy and total internal reflection microscopy (TIRM), although all of them induce evanescent waves in the imaging process (Supplemental Video 1). TIRF uses evanescent waves to stimulate fluorophores labeled in the sample. The fluorescent light is detected as signals and forms a totally incoherent image with high vertical resolution but diffraction-limited lateral resolution. TIRM uses coherent evanescent illumination to achieve lateral subwavelength imaging; however, it suffers from a low SNR, because the scattered signal light has the same wavelength as the external input laser. NWRIM combines the advantages of TIRF and TIRM and adopts a totally different way to stimulate evanescent waves: The evanescent waves are stimulated by the fluorescent NWR. The cooperation between the spatial frequency shift and the Stokes frequency shift in NWRIM enables the super-lateral resolution with a wide FOV, as well as suppressing the background noise by selecting the signal using a bandpass filter. What is more, the partial coherence of the NW emission also helps to prevent coherent artifacts and improve the speckle-free full-field imaging [38]. The ring-shape design of the NW in NWRIM makes it convenient to achieve omnidirectional illumination for 2D imaging. In addition, the nanofootprint of the fluorescent NW leads to a much smaller device size. Compared with structured illumination microscopy [39], another wide-field far-field microscopy, NWRIM enables label-free observation and possesses a greater potential to improve the spatial resolution by using the near-field evanescent waves rather than the far-field propagation waves for illumination. Compared with other far-field nanoscopy imaging methods, such as the hyperlens [14], microsphere or nanofiber contact lens [13,37], and nanorod array [17] technologies, NWRIM significantly improves the FOV, which has reached up to around 1000 μm^2 in a single shot [Figs. 3(d), 4(g), and 5(b)].

Nowadays, with the developments in cell biology, on-chip industry, and molecular- or atomic-scale research, the demands for fast, wide-field, label-free, and low-cost subdiffraction microscopy are increasing dramatically [13–18,40]. We first applied NWR to examine Blu-ray disks with 150 nm tracks. No storage structure is visible under conventional illumination in Fig. 5(a). In contrast, under NW illumination [Fig. 5(b)], gratinglike structures in the blank region and storage dots in the recorded region are both apparent. Then, we applied NWRIM to image an integrated chip. In the dense areas of the integrated chip, the distance among the metal wires is very small, especially in the inner layers. Using NWRIM, all the closely arranged wires can be resolved [Fig. 5(d)], but they are severely blurred under conventional illumination [Fig. 5(c)]. Finally, we observed some biological samples without applying any dye or label (Fig. S19). The image captured using NW illumination reveals subdiffraction images of fat particles in cytoplasm and multiple-layer structures in a 3T3 l1 cell, whose capability may prove useful in studying cancer and assessing drug effects.

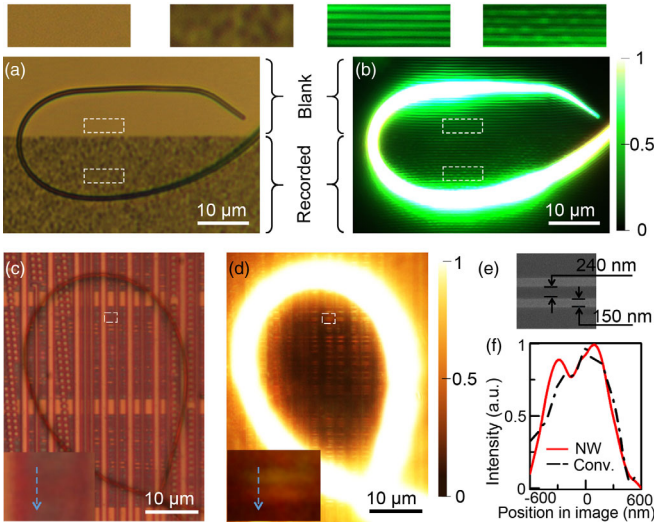

FIG. 5. NWRIM images of Blu-ray disks and integrated circuits. (a),(b) Conventional (a) and NWRIM (b) images of a Blu-ray disk. Boxed regions are magnified on the top insets. (c), (d) Conventional (c) and NWRIM (d) images of an integrated chip. Boxed regions are magnified in the left bottom insets, and the SEM and cross-sectional intensity distribution along the blue arrows are shown in (e) and (f). NWRIM and conventional illumination are abbreviated as NW and Conv., respectively. NA = 0.85.

In addition to its outstanding subdiffraction imaging, NWRIM is remarkably cost-effective. Millions of NWs can be fabricated in a single growth batch. NWRIM and conventional microscopy systems are also easily integrated. The substrate with a thin film is basically a special microscope slide. We simply put the sample on this slide and pump an NW ring to illuminate it. The subdiffraction imaging can then be achieved easily with a standard objective. The good compatibility enables this design to be used as a compact illumination module giving a super resolving ability to conventional microscopy.

In order to explore the integration of NWRIM with conventional microscopy, we experimentally used objectives with different NAs (0.6–0.9) to collect the scattered light and form far-field images. The object was a V-shaped structure (Fig. S20), whose two branches diverged gradually from nearly zero to several hundred nanometers. All the objectives successfully resolved a subdiffraction segment of the V-shaped structure under the NW illumination, while interestingly, a diffraction-unlimited part could blur when NA is small, resulting from the objective's incapability to collect two or more different diffraction orders simultaneously [41] (S5). To broaden the collected spatial frequency range and understand the full structure information of an object, we can combine the spatial frequencies provided by images captured under illuminations with multiple TWVs, e.g., evanescent wave illumination at multiple wavelengths. A super resolution image without a blur region and distortion has been successfully achieved for the V-shaped structure in the simulations based on this multiple-wavelength-illumination method (Fig. S25). In future experiments, we can use an NW with a graded band gap [42,43] or nonlinear properties [6,44] for illumination and capture the far-field images at several different wavelengths for imaging reconstruction. One thing to be noted is, as NWRIM is a scattering- or diffraction-based imaging method, a refractive index fluctuation is essential for high SNR imaging. And fabrication of high-quality film is needed for the dependence of FOV on the light propagation distance in the film.

In conclusion, this Letter reports the first nanoscale light-source-based wide-field and far-field label-free subdiffraction imaging by hybridizing fluorescent ring-shaped NWs with subwavelength film waveguides. Subdiffraction images of 2D patterns, integrated chips, Blu-ray disks, and biological cells were successfully obtained. The illuminating wavelength can be easily varied by using different kinds of NWs, and the detectable spatial frequency range can be broadened correspondingly. The resolvability can be further improved by increasing the TWV of the evanescent wave with a higher refractive index material, e.g., metamaterials, as the film waveguide. These observations and measurements on various subdiffraction-limited samples illustrate that our method significantly expands the flexibility of nanoscale light sources for applications in biomedicine, on-chip industry, materials science, and elsewhere.

The authors thank Professor Fangwei Wang, Yuanpeng Wu, Zongyin Yang, and Liang Xu for preparing NW samples and objects for imaging and thank Professor Hongsheng Chen, Professor Kebin Shi, and Peng Xiu for helpful discussions. The authors also thank Professor James Ballard for his close editorial review of the article. This work is supported by National Key Basic Research Program of China (No. 2015CB352003 and No. 2013CB 328703), National Natural Science Foundation of China (No. 51672245, No. 51372220, and No. 61177062), the Fundamental Research Funds for the Central Universities, the Program for Zhejiang Leading Team of S&T Innovation, and the Fundamental Research Funds for the Central Universities.

*Corresponding author.
qingyang@zju.edu.cn
†liuxu@zju.edu.cn

[1] R. M. Dickson, A. B. Cubitt, R. Y. Tsien, and W. E. Moerner, Nature (London) **388**, 355 (1997).
[2] E. Betzig, G. H. Patterson, R. Sougrat, O. W. Lindwasser, S. Olenych, J. S. Bonifacino, M. W. Davidson, J. Lippincott-Schwartz, and H. F. Hess, Science **313**, 1642 (2006).
[3] S. W. Hell, Science **316**, 1153 (2007).
[4] X. Zhuang, Nat. Photonics **3**, 365 (2009).
[5] E. Betzig and J. K. Trautman, Science **257**, 189 (1992).
[6] Y. Nakayama, P. J. Pauzauskie, A. Radenovic, R. M. Onorato, R. J. Saykally, J. Liphardt, and P. Yang, Nature (London) **447**, 1098 (2007).
[7] D. W. Pohl, W. Denk, and M. Lanz, Appl. Phys. Lett. **44**, 651 (1984).
[8] E. J. Sánchez, L. Novotny, and X. S. Xie, Phys. Rev. Lett. **82**, 4014 (1999).
[9] R. Bachelot, P. Gleyzes, and A. C. Boccara, Opt. Lett. **20**, 1924 (1995).
[10] T. Yano, P. Verma, Y. Saito, T. Ichimura, and S. Kawata, Nat. Photonics **3**, 473 (2009).
[11] J. Steidtner and B. Pettinger, Phys. Rev. Lett. **100**, 236101 (2008).
[12] L. Wang and X. G. Xu, Nat. Commun. **06**, 1 (2016).
[13] Z. Wang, W. Guo, L. Li, B. Luk'yanchuk, A. Khan, Z. Liu, Z. Chen, and M. Hong, Nat. Commun. **2**, 218 (2011).
[14] J. Rho, Z. Ye, Y. Xiong, X. Yin, Z. Liu, H. Choi, G. Bartal, and X. Zhang, Nat. Commun. **1**, 143 (2010).
[15] Z. Liu, H. Lee, Y. Xiong, C. Sun, and X. Zhang, Science **315**, 1686 (2007).
[16] J. Yao, L. Wang, C. Li, C. Zhang, and L. V. Wang, Phys. Rev. Lett. **112**, 014302 (2014).
[17] S. Kawata, A. Ono, and P. Verma, Nat. Photonics **2**, 438 (2008).
[18] G. D. Byrne, M. C. Pitter, J. Zhang, F. H. Falcone, S. Stolnik, and M. G. Somekh, J. Microsc. **231**, 168 (2008).
[19] P. R. West, S. Ishii, G. V. Naik, N. K. Emani, V. M. Shalaev, and A. Boltasseva, Laser Photonics Rev. **4**, 795 (2010).
[20] B. Tian, T. Cohen-Karni, Q. Qing, X. Duan, P. Xie, and C. M. Lieber, Science **329**, 830 (2010).
[21] D. D. D. Ma, C. S. Lee, F. C. K. Au, S. Y. Tong, and S. T. Lee, Science **299**, 1874 (2003).

[22] L. Tong, R. R. Gattass, J. B. Ashcom, S. He, J. Lou, M. Shen, I. Maxwell, and E. Mazur, Nature (London) **426**, 816 (2003).
[23] Q. Qing, Z. Jiang, L. Xu, R. Gao, L. Mai, and C. M. Lieber, Nat. Nanotechnol. **9**, 142 (2014).
[24] Q. Yang, W. Wang, S. Xu, and Z. L. Wang, Nano Lett. **11**, 4012 (2011).
[25] M. Law, L. E. Greene, J. C. Johnson, R. Saykally, and P. Yang, Nat. Mater. **4**, 455 (2005).
[26] A. Kolmakov, Y. Zhang, G. Cheng, and M. Moskovits, Adv. Mater. **15**, 997 (2003).
[27] L. Tong, J. Lou, and E. Mazur, Opt. Express **12**, 1025 (2004).
[28] P. Norvig, D. A. Relman, D. B. Goldstein, D. M. Kammen, D. R. Weinberger, L. C. Aiello, G. Church, J. L. Hennessy, J. Sachs, A. Burrows, G. P. Pisano, J. R. Goldstein, P. Anastas, R. Klausner, D. Baltimore, D. R. Montgomery, T. M. Baer, N. P. Bigelow, R. D. Holt, and J. K. Nicholson, Nature (London) **463**, 26 (2010).
[29] V. J. Sorger and X. Zhang, Science **333**, 709 (2011).
[30] See Supplemental Material at http://link.aps.org/supplemental/10.1103/PhysRevLett.118.076101 for additional experimental results, simulations and calculations.
[31] M. H. Huang, S. Mao, H. Feick, H. Yan, Y. Wu, H. Kind, E. Weber, R. Russo, and P. Yang, Science **292**, 1897 (2001).
[32] X. Duan, Y. Huang, R. Agarwal, and C. M. Lieber, Nature (London) **421**, 241 (2003).
[33] C. Pan, L. Dong, G. Zhu, S. Niu, R. Yu, Q. Yang, Y. Liu, and Z. L. Wang, Nat. Photonics **7**, 752 (2013).
[34] M. Born and E. Wolf, *Principles of Optics: Electromagnetic Theory of Propagation, Interference and Diffraction of Light* (Cambridge University Press, Cambridge, 1999), Chap. 13.
[35] J. W. Goodman, *Introduction to Fourier Optics* (Roberts and Company, 2005).
[36] G. Chen, J. Wu, Q. Lu, H. R. Gutierrez, Q. Xiong, M. E. Pellen, J. S. Petko, D. H. Werner, and P. C. Eklund, Nano Lett. **8**, 1341 (2008).
[37] X. Hao, X. Liu, C. Kuang, Y. Li, Y. Ku, H. Zhang, H. Li, and L. Tong, Appl. Phys. Lett. **102**, 013104 (2013).
[38] B. Redding, M. A. Choma, and H. Cao, Nat. Photonics **6**, 355 (2012).
[39] M. G. L. Gustafsson, J. Microsc. **198**, 82 (2000).
[40] L. Shao, X.-F. Jiang, X.-C. Yu, B.-B. Li, W. R. Clements, F. Vollmer, W. Wang, Y.-F. Xiao, and Q. Gong, Adv. Mater. **25**, 5616 (2013).
[41] M. Born and E. Wolf, *Principles of Optics: Electromagnetic Theory of Propagation, Interference and Diffraction of Light* (Cambridge University Press, Cambridge, 1999), Chap. 8.
[42] J. Li, C. Meng, Y. Liu, X. Wu, Y. Lu, Y. Ye, L. Dai, L. Tong, X. Liu, and Q. Yang, Adv. Mater. **25**, 833 (2013).
[43] Z. Yang, D. Wang, C. Meng, Z. Wu, Y. Wang, Y. Ma, L. Dai, X. Liu, T. Hasan, X. Liu, and Q. Yang, Nano Lett. **14**, 3153 (2014).
[44] H. Yu, W. Fang, X. Wu, X. Lin, L. Tong, W. Liu, A. Wang, and Y. R. Shen, Nano Lett. **14**, 3487 (2014).